



On the design of piezoelectric MEMS scanning mirror for large reflection area and wide scan angle

Hao-Chien Cheng^{a,b}, Shi-Chi Liu^c, Chih-Chen Hsu^a, Hung-Yu Lin^c, Fuchi Shih^a,
Mingching Wu^b, Kai-Chih Liang^b, Mei-Feng Lai^a, Weileun Fang^{a,c,*}

^a Institute of Nano Engineering and MicroSystem, National Tsing Hua Univ., Hsinchu, Taiwan

^b Coretronic MEMS Corporation, Miaoli, Taiwan

^c Power Mechanical Engineering Department, National Tsing Hua Univ., Hsinchu, Taiwan

ARTICLE INFO

Keywords:

Piezoelectric actuator
PZT film
Micro scanner
Scanning mirror

ABSTRACT

This study designs and implements the piezoelectric MEMS scanning mirror with large scan angle and reflection area for light beam manipulating applications. In this design, the scanning mirror has a large mirror plate (3 mm in diameter) supported by two T-shape torsional springs. The U-shape piezoelectric cantilever acts as the actuator to drive the scanning mirror through the transmission spring. The analytical model is established to provide the design guideline of transmission spring to increase the scan angle. In application, the proposed designs are fabricated on the SOI (silicon on insulator) wafer deposited with the PZT film. Measurements indicate the fabricated mirror could reach an optical scan angle of 140-degree (mechanical scan angle of ± 35 -degree) when driving at its resonant frequency of 1.5 kHz with a unipolar driving voltage of 42 V. Moreover, no vacuum environment is required for the presented scanning mirror to achieve the above scan angle. This is an extremely large optical scan angle for the MEMS scanner with a mirror plate of 3 mm in diameter. In addition, another U-shape piezoelectric cantilever serves as the position sensor to detect the scan angle of mirror plate. The sensing signals show good linearity with the scan angles and can be exploited as the feedback control. Measurements also demonstrate that the micro scanner could withstand 1500 g shock loading, and the deviation of scan angle is less than 10% after the cycling test under 10 V_{pp} resonant driving in 95%RH and room temperature for 0.2 billion cycles.

1. Introduction

The optical scanning mirror for light beam steering has been applied in broad fields such as scientific tools, medical instruments, etc. The microelectromechanical system (MEMS) technology has demonstrated its capability to miniaturize the optical scanning mirror. Many advantages, for example higher scanning frequency, lower power consumption and cost, smaller device, etc., could be achieved by using the MEMS scanning mirror. The MEMS scanning mirror could also be employed to steer the laser beam to enhance light intensity for sensing and display [1–4]. Texas Instrument successfully demonstrates the commercial product by using the MEMS scanning mirror array [5,6]. To date, the MEMS scanning mirror can find wide applications in the projection display [7], optical switch [8], biomedical imaging [9], light detection, and ranging (LiDAR) system [10,11], and so on. Consequently, the MEMS scanning mirror is considered as one of the promising

components to realize the head-up display and the LiDAR for the booming autonomous vehicles.

The existing MEMS scanning mirror are mainly driven through electromagnetically or electrostatically approaches [12–19]. The micromachining processes for electrostatic MEMS scanning mirrors are relatively simple and mature. Various electrostatic scanning mirrors have been demonstrated using the SOI wafer processes [12], and the poly-Si fabrication platforms [13]. The gap-closing and vertical comb electrodes together with different novel transmission mechanisms are exploited to enhance the performances of scanning mirrors [13–15]. For electrostatic scanning mirrors, smaller gaps between electrodes are frequently designed to decrease the driving voltage or increase the scan angle of mirror. However, scanning mirrors are often operating in harsh environments with vibration and shock for autonomous vehicle applications, and hence the pull-in effect will be a critical concern in this regard [16]. The electromagnetic force is another option to drive

* Corresponding author at: Power Mechanical Engineering Department, National Tsing Hua Univ., Hsinchu, Taiwan.

E-mail addresses: howard.cheng@coretronicmems.com (H.-C. Cheng), fang@pme.nthu.edu.tw (W. Fang).

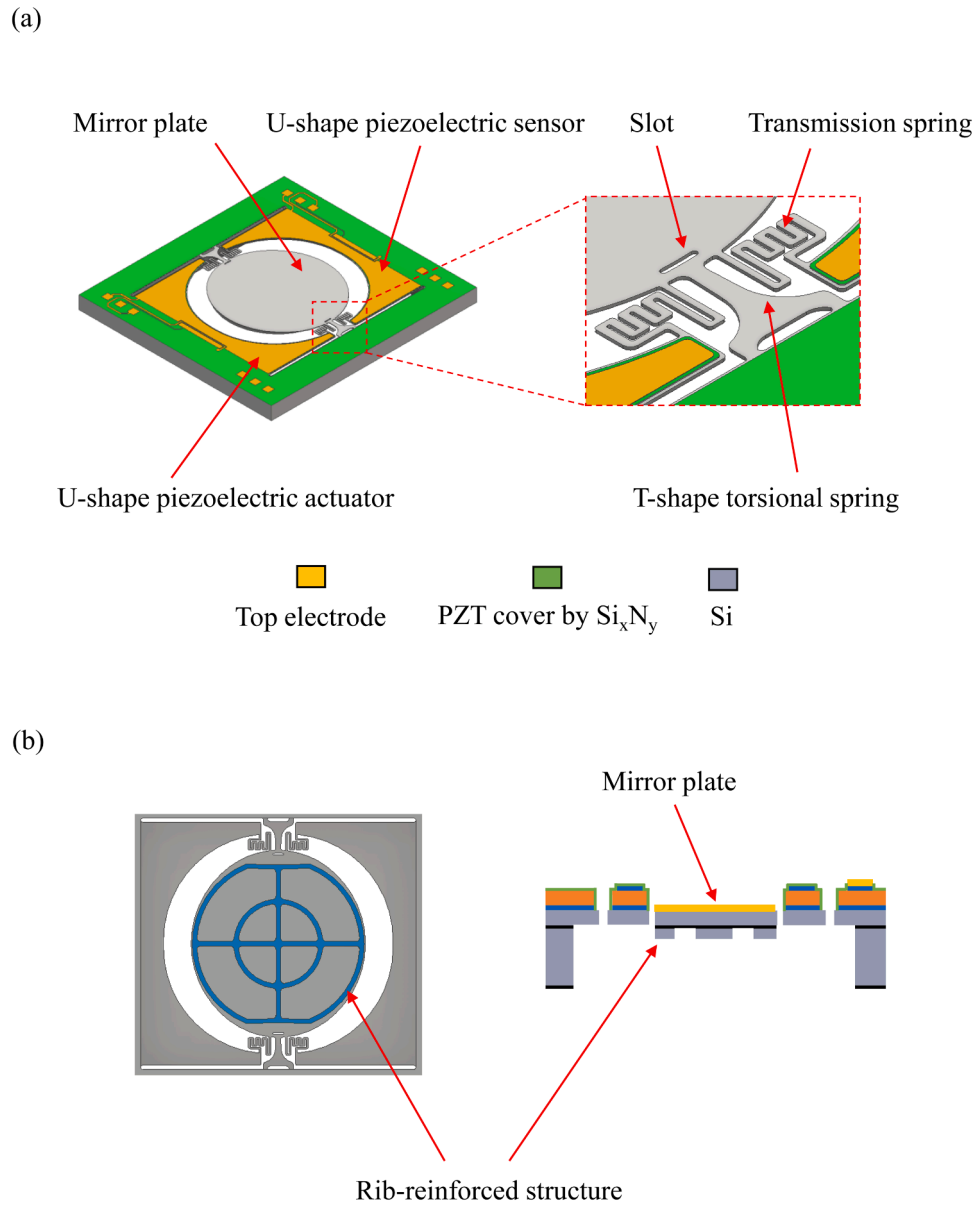


Fig. 1. (a) Isometric illustration of the proposed scanning mirror and the zoom-in diagram of transmission spring and T-shape torsional spring, and (b) the backside and cross section views of the proposed scanning mirror.

scanning mirrors with decent actuation loads [17–20]. To enlarge the actuation loads for mirror, the assembly of magnets and the coil winding outside the mirror chip are frequently required [21]. Thus, extra efforts and cost are needed for these non-batched assembly processes, and the device size is also relatively large after assembly. Moreover, the power consumption and temperature rising are other concerns for the electromagnetic scanning mirrors [21]. The MEMS actuators and scanning mirrors driven by the piezoelectric thin films have also been investigated [21]. The characteristic of piezoelectric actuation could prevent the pull-in and temperature rising effects. The piezoelectric MEMS scanning mirror also has relatively low driving voltage and power consumption. Since the PZT (Lead-Zirconate-Titanate) thin film exhibits a relatively large piezoelectric coefficient [22], it is considered as an excellent candidate for the implementation of piezoelectric scanning mirrors. The quality and availability of the PZT films are gradually improved in recent years. Designs of PZT MEMS scanning mirrors with different structures, actuators, driving and sensing electrodes, and so on have

been reported [23–26]. For example, the meandering actuator and large mirror plate are designed for different applications [23,24]. The PZT scanning mirror with special driving electrodes or equipped with sensing electrodes are reported in [25,26].

This study will focus on the development of piezoelectric MEMS scanning mirror which has the potential to apply in the vehicle LiDAR. In general, high luminance and large field-of-view are important specifications for the vehicle LiDAR [27]. In this regard, the large reflection area (mirror plate) and wide scan angle are two design requirements for the MEMS scanning mirror. However, it is not straightforward to design the MEMS scanning mirror to exhibit both large mirror plate and scan angle [28]. The approach to combine multiple scanning mirrors to enlarge the field of view (FOV) has been presented in [28]. To implement this design, multiple scanning mirrors with independent control system are required for each scanning mirror. Various approaches to design actuation schemes and mechanical structures to increase the scan angle have also been reported [29–33]. As discussed in [29,30], the

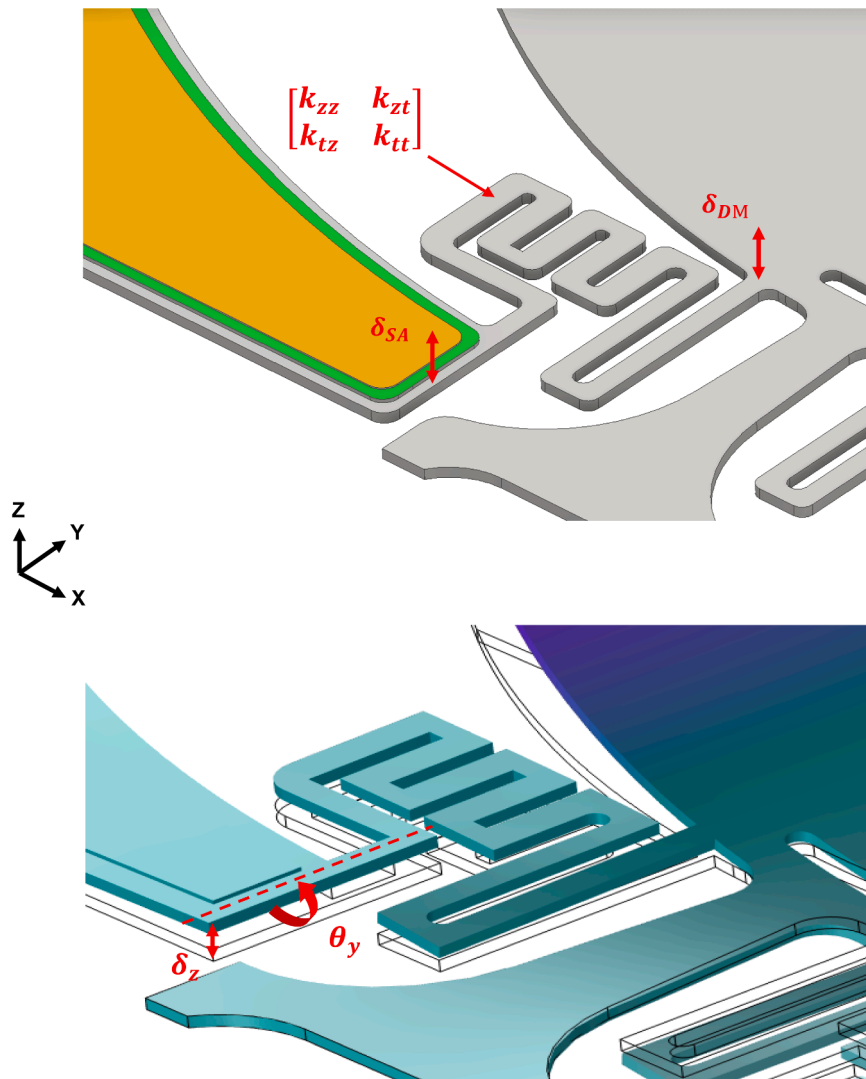
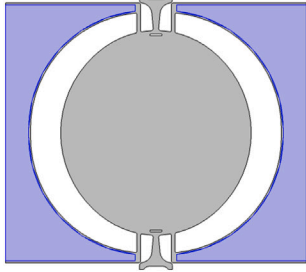
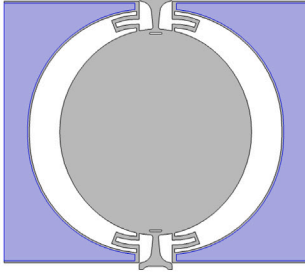
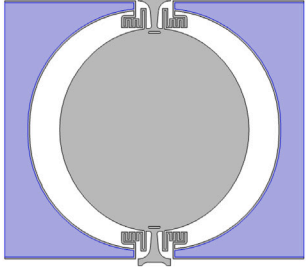


Fig. 2. The physical model of the proposed scanning mirror design, particularly the transmission spring, to determine the linear static displacement δ_{SA} of the actuator tip, and further find out the dynamic displacement of the mirror plate δ_{DM} . During actuation, the U-shape actuator tip is allowed to have the linear displacement δ_z about z-axis and the angular displacement θ_y about y-axis, so that the transmission spring will be deformed to move the mirror plate.

Table 1

Summarized static tip displacement δ_{SA} of the U-shape actuator and the maximum stress of the T-shape torsional spring for both reference and proposed designs. The analysis and simulation results are included for comparison.

	Reference design A	Reference design B	Proposed design
Design			
Theoretical δ_{SA}	5.20 μm	9.61 μm	11.32 μm
Simulated δ_{SA}	6.53 μm	10.8 μm	11.06 μm
Error	20%	11%	2.3%
Maximum stress/ mechanical angle	168.74 MPa/$^\circ$	112.85 MPa/$^\circ$	89.43 MPa/$^\circ$

meandering structures deposited with PZT film are used as the spring and actuator to enlarge the scan angle. The PZT film on large supporting frame has been employed to drive the mirror plate and large scan angle is achieved when operating at the out of phase resonant mode [31]. The approach to exploit connection springs between the actuators and the mirror plate to increase the scanning angle have been reported [32,33]. However, it remains challenging to achieve large mirror plate and scan angle simultaneously. To meet the above goals, this study leverages the concept in [32,33], to establish the analytical model as the design guideline for connection springs. After that, the finite element method (FEM) simulation is used to fine tune the structure design. In application, this study will demonstrate the design of a scanning mirror with a large reflection area (a mirror plate with 3 mm in diameter). The designs are implemented by the micromachining processes with the piezoelectric film on the SOI wafer. Measurements indicate that the fabricated MEMS scanner with a 3 mm diameter mirror plate have a 140-degree scan angle in air (not in vacuum) which could meet the application specifications.

2. Design concepts and principles

Fig. 1 shows the schema of the proposed design. As indicated in Fig. 1a, the scanning mirror is consisted of a mirror plate supported by two T-shape torsional springs which anchored to the substrate. In addition, the scanning mirror is driven by the U-shape cantilever piezoelectric actuator through the transmission springs. Another U-shape cantilever acts as the piezoelectric sensor to detect the scan angle of the mirror plate. The circular mirror plate is 3 mm in diameter to offer a large reflection area, and the slots on the mirror plate are designed to

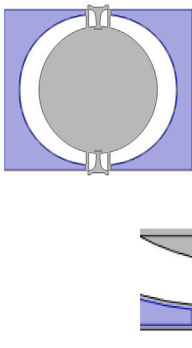
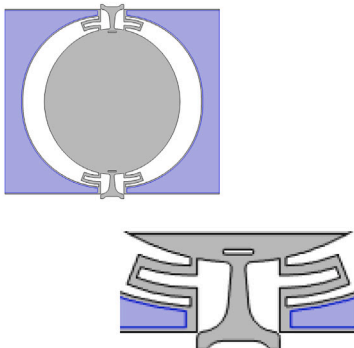
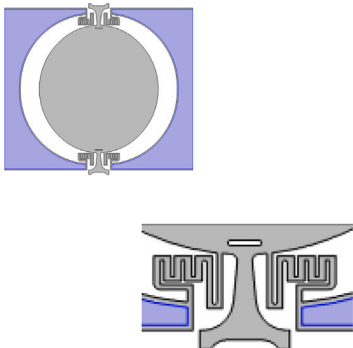
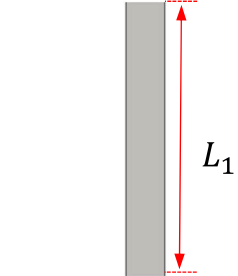
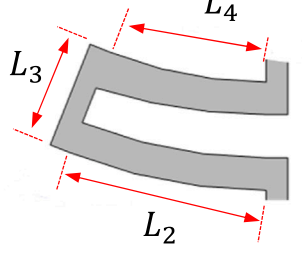
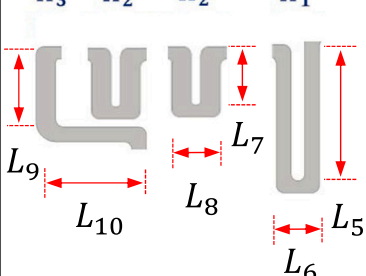
reduce the stress on torsional spring. As the backside and cross-section views indicated in Fig. 1b, the mirror plate with rib-reinforced structures could maintain the stiffness to reduce dynamic deformation during operation [35,36]. The T-shape torsional springs are exploited to reduce the torsional stiffness to increase the scan angle, while maintaining sufficient amount of robustness in out-of-plane direction to prevent failure when device is under severe shock or vibration. In this design, one of the U-shape unimorph piezoelectric cantilevers is employed to excite the scanning mirror. The U-shape cantilever will be bent by the piezoelectric film to actuate the mirror when a driving signal input into the scanner. On the other hand, an output signal can be detected from the piezoelectric film when the sensing U-shape cantilever bent by the rotating mirror. Note the vibration energy is transmitted from the actuator to the mirror plate through the transmission springs. Thus, the performances of the presented scanning mirror are influenced by the design of the transmission springs, the T-shape springs, and the U-shape actuators. This study will focus on the design of the transmission springs. In this regard, the analytical model will be established to evaluate and decide the design of transmission springs. After that, the finite element simulations are used to predict the dynamic characteristics of the scanning mirror design.

2.1. Analytical solution

The schematic illustrations in Fig. 2 depict the model used to derive the analytical solution. The top and bottom illustrations respectively show the scanning mirror before and after actuation. Various important parameters are also marked in figures. To simplify the analytical model, this study assumes that the dynamic system is formed by the mirror

Table 2

Summarized of the stiffness matrix for both reference and proposed designs. Where I_{ij} is the moment of inertia of the springs, and the first subscription i depicts the direction of neutral axis, the second subscription j indicates the direction of the beam; J_k is torsional moment of inertia of the springs, and the subscription k represents the direction of perpendicular axis. In addition, E and G are respectively the elastic modulus and the shear modulus.

	Reference design A	Reference design B	Proposed design
Design			
k_{zz}	279.1 N/m $3EI_{x,L_1}/L_1^3$	75.58 N/m $B(2B_1 + B_4)$	67.33 N/m $K_{total}^{-1} = K_1^{-1} + 2K_2^{-1} + K_3^{-1}$
k_{tt}	$1.09 \times 10^{-5} \text{ N} \cdot \text{m}$ GJ_{L_1}/L_1	$7.87 \times 10^{-6} \text{ N} \cdot \text{m}$ $B(\frac{2L_2^2}{3}B_1 + \frac{L_3^2}{3}B_2 + L_3^2B_3 + L_2^2B_4)$	$2.15 \times 10^{-6} \text{ N} \cdot \text{m}$ $K_{total}^{-1} = K_1^{-1} + 2K_2^{-1} + K_3^{-1}$
k_{zt}/k_{tz}	0	$2.11 \times 10^{-2} \text{ N}$ $B(2L_2B_1 + L_2B_4)$	$9.49 \times 10^{-3} \text{ N}$ $K_{total}^{-1} = K_1^{-1} + 2K_2^{-1} + K_3^{-1}$
Dimensions of the Transmission Springs	Planar dimensions		
	 The width of L_1 is w_1	 The width of L_2, L_4 is w_2 The width of L_3 is w_3	 The width of L_i is w_i where $i = 5 \sim 10$
	Thickness		
	t_1	t_1	t_1

(continued on next page)

Table 2 (continued)

Reference A	$k_{zz} = \frac{3EI_{xL_1}}{L_1^3} \quad k_{tt} = \frac{GJ_{L_1}}{L_1} \quad k_{zt} = 0 \quad I_{xL_1} = \int_A y^2 dA \quad J_{L_1} = \int_A r^2 dA$															
Reference B	$k_{zz} = B(2B_1 + B_4) \quad k_{tt} = B\left(\frac{2L_2^2}{3}B_1 + \frac{L_3^2}{3}B_2 + L_3^2B_3 + L_2^2B_4\right)$ $k_{zt} = B(2L_2B_1 + L_2B_4)$ $B = \frac{1}{\frac{L_2^2B_1^2}{3} + \frac{2L_3^2B_1B_2}{3} + \frac{2L_2^2B_1B_4}{3} + 2L_2L_3B_1B_3 + \frac{L_3^2B_2B_4}{3} + 2L_3^2B_3B_4}$ $B_1 = \frac{L_2}{(EI_{xL_2})} \quad B_2 = \frac{L_3}{(EI_{yL_3})} \quad B_3 = \frac{L_2}{(GJ_{L_2})} \quad B_4 = \frac{L_3}{(GJ_{L_3})}$															
Proposed	$K_1 = Q \begin{bmatrix} (2Q_1 + Q_4) & (L_5Q_1 + L_5Q_4) \\ (L_5Q_1 + L_5Q_4) & \left(\frac{2L_5^2}{3}Q_1 + \frac{L_6^2}{3}Q_2 + L_6^2Q_3 + L_5^2Q_4\right) \end{bmatrix}$ $Q = \frac{1}{\frac{L_5^2Q_1^2}{3} + \frac{2L_6^2Q_1Q_2}{3} + \frac{2L_5^2Q_1Q_4}{3} + 2L_5L_6Q_1Q_3 + \frac{L_6^2Q_2Q_4}{3} + 2L_6^2Q_3Q_4}$ $Q_1 = \frac{L_5}{(EI_{xL_5})} \quad Q_2 = \frac{L_6}{(EI_{yL_6})} \quad Q_3 = \frac{L_5}{(GJ_{L_5})} \quad Q_4 = \frac{L_6}{(GJ_{L_6})}$ $K_2 = R \begin{bmatrix} (2R_1 + R_4) & (L_7R_1 + L_7R_4) \\ (L_7R_1 + L_7R_4) & \left(\frac{2L_7^2}{3}R_1 + \frac{L_8^2}{3}R_2 + L_8^2R_3 + L_7^2R_4\right) \end{bmatrix}$ $R = \frac{1}{\frac{L_7^2R_1^2}{3} + \frac{2L_8^2R_1R_2}{3} + \frac{2L_7^2R_1R_4}{3} + 2L_7L_8R_1R_3 + \frac{L_8^2R_2R_4}{3} + 2L_8^2R_3R_4}$ $R_1 = \frac{L_7}{(EI_{xL_7})} \quad R_2 = \frac{L_8}{(EI_{yL_8})} \quad R_3 = \frac{L_7}{(GJ_7)} \quad R_4 = \frac{L_8}{(GJ_{L_8})}$ $K_3 = S \begin{bmatrix} (S_1 + S_4) & \left(\frac{L_9S_1}{2} + L_9S_4\right) \\ \left(\frac{L_9S_1}{2} + L_9S_4\right) & \left(\frac{L_9^2}{3}S_1 + \frac{L_{10}^2}{3}S_2 + L_9^2S_4\right) \end{bmatrix}$ $S = \frac{1}{\frac{L_9^2S_1^2}{12} + \frac{L_9^2S_1S_4}{3} + \frac{2L_{10}^2S_1S_2}{3} + \frac{L_{10}^2S_2S_4}{3}}$ $S_1 = \frac{L_9}{(EI_{xL_9})} \quad S_2 = \frac{L_{10}}{(EI_{yL_{10}})} \quad S_3 = \frac{L_9}{(GJ_{L_9})} \quad S_4 = \frac{L_{10}}{(GJ_{L_{10}})}$															
Value of Dimension	<table style="width: 100%; border-collapse: collapse;"> <tr> <td style="width: 33%;">$L_5 = 302 \mu\text{m}$</td> <td style="width: 33%;">$L_6 = 88 \mu\text{m}$</td> <td style="width: 33%;">$L_7 = 145 \mu\text{m}$</td> </tr> <tr> <td>$L_8 = 100 \mu\text{m}$</td> <td>$L_9 = 195 \mu\text{m}$</td> <td>$L_{10} = 196 \mu\text{m}$</td> </tr> <tr> <td>$w_5 = 30 \mu\text{m}$</td> <td>$w_6 = 25 \mu\text{m}$</td> <td>$w_7 = 40 \mu\text{m}$</td> </tr> <tr> <td>$w_8 = 25 \mu\text{m}$</td> <td>$w_9 = 40 \mu\text{m}$</td> <td>$w_{10} = 30 \mu\text{m}$</td> </tr> <tr> <td>$t_1 = 15 \mu\text{m}$</td> <td></td> <td></td> </tr> </table>	$L_5 = 302 \mu\text{m}$	$L_6 = 88 \mu\text{m}$	$L_7 = 145 \mu\text{m}$	$L_8 = 100 \mu\text{m}$	$L_9 = 195 \mu\text{m}$	$L_{10} = 196 \mu\text{m}$	$w_5 = 30 \mu\text{m}$	$w_6 = 25 \mu\text{m}$	$w_7 = 40 \mu\text{m}$	$w_8 = 25 \mu\text{m}$	$w_9 = 40 \mu\text{m}$	$w_{10} = 30 \mu\text{m}$	$t_1 = 15 \mu\text{m}$		
$L_5 = 302 \mu\text{m}$	$L_6 = 88 \mu\text{m}$	$L_7 = 145 \mu\text{m}$														
$L_8 = 100 \mu\text{m}$	$L_9 = 195 \mu\text{m}$	$L_{10} = 196 \mu\text{m}$														
$w_5 = 30 \mu\text{m}$	$w_6 = 25 \mu\text{m}$	$w_7 = 40 \mu\text{m}$														
$w_8 = 25 \mu\text{m}$	$w_9 = 40 \mu\text{m}$	$w_{10} = 30 \mu\text{m}$														
$t_1 = 15 \mu\text{m}$																

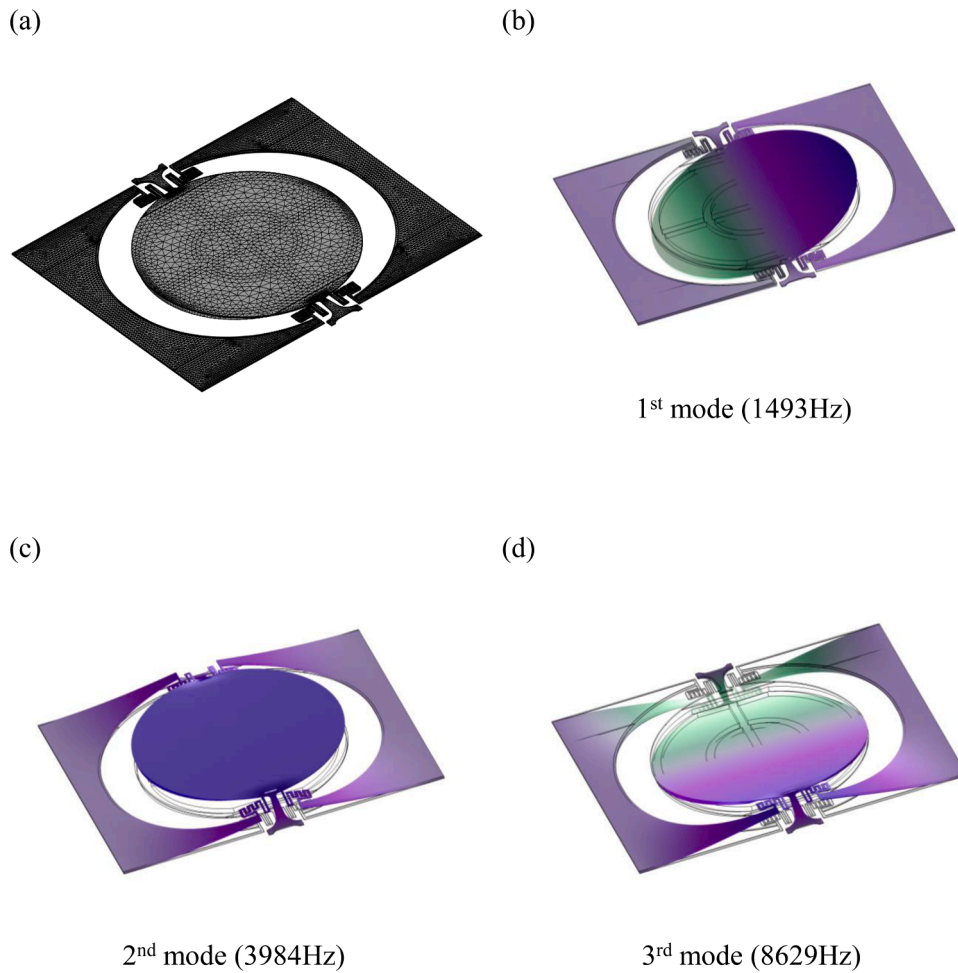


Fig. 3. The FEM simulation results: (a) typical model used in FEM simulation, (b) the 1st mode of the proposed design, featuring angular motion (about the T-shape torsional spring) of mirror plate, (c) the 2nd mode of the proposed design, featuring piston motion of the mirror plate, and (d) the 3rd mode of the proposed design, featuring rocking motion of the device.

plate, and the T-shape and the transmission springs. In addition, the dynamic system is driven by the U-shape piezoelectric actuator through the transmission springs. Thus, the analytical model is established to find the transmission spring design to achieve a larger dynamic response of mirror plate δ_{DM} . For the dynamic system driven by the actuator in Fig. 2, the dynamic response of mirror plate δ_{DM} is expressed as [37],

$$\delta_{DM} = \delta_{DA}TR \quad (1)$$

where δ_{DA} is the dynamic displacements applied on the mirror by the actuator, and TR is the transmission ratio of the dynamic system. The parameter TR determines the efficiency of vibration energy transmission between actuators and mirror plate. In general, TR is dependent on the operating frequency. Moreover, the dynamic displacement of the actuator δ_{DA} can be denoted as,

$$\delta_{DA} = \delta_{SA}QF \quad (2)$$

where δ_{SA} and QF are respectively the static displacement and the quality factor of the piezoelectric actuator. From Eqs. (1) and (2), the dynamic displacement of the mirror δ_{DM} (i.e. scan angle) is proportional to the static displacement of the piezoelectric actuator δ_{SA} . Consequently, this study will design the transmission springs to enlarge the δ_{SA} .

As shown in Fig. 2, the actuator is flexible to perform the linear tip displacement δ_z in z-axis and the angular tip displacement θ_y about the

y-axis. The rest of the tip displacements can be ignored for this actuator. The transmission spring, with one end fixed to the actuator, is also having the tip displacements δ_z and θ_y . Thus, the deformed transmission spring will generate elastic restoring loads acting on the connection between the spring and the actuator,

$$\begin{bmatrix} F_s \\ M_s \end{bmatrix} = \begin{bmatrix} k_{zz} & k_{zt} \\ k_{tz} & k_{tt} \end{bmatrix} \begin{bmatrix} \delta_z \\ \theta_y \end{bmatrix} \quad (3)$$

where F_s is the force in the z-axis and M_s is the bending moment about the y-axis, and k_{zz} , k_{zt} , k_{tz} , and k_{tt} are the stiffness terms of the transmission spring. Note the first subscript of the stiffness term denotes the direction of strain, and the second subscript denotes the direction of applied force. Moreover, in this study, the piezoelectric film is employed to generate a force F_p on the actuator. The force F_p can be found through the integration over the length L of the piezoelectric thin film using the Hamilton's principle [38],

$$F_p = e_{31}V \frac{w}{L} Z_m \quad (4)$$

where e_{31} is the piezoelectric coefficient of the PZT film, V is the input voltage, w is the width of the PZT film, and Z_m is the distance between the neutral axis and piezoelectric thin film. In addition, the residual stress of PZT film also applies an equivalent bending moment M_σ on the actuator. The strain energy contributed by the thin film residual stress σ

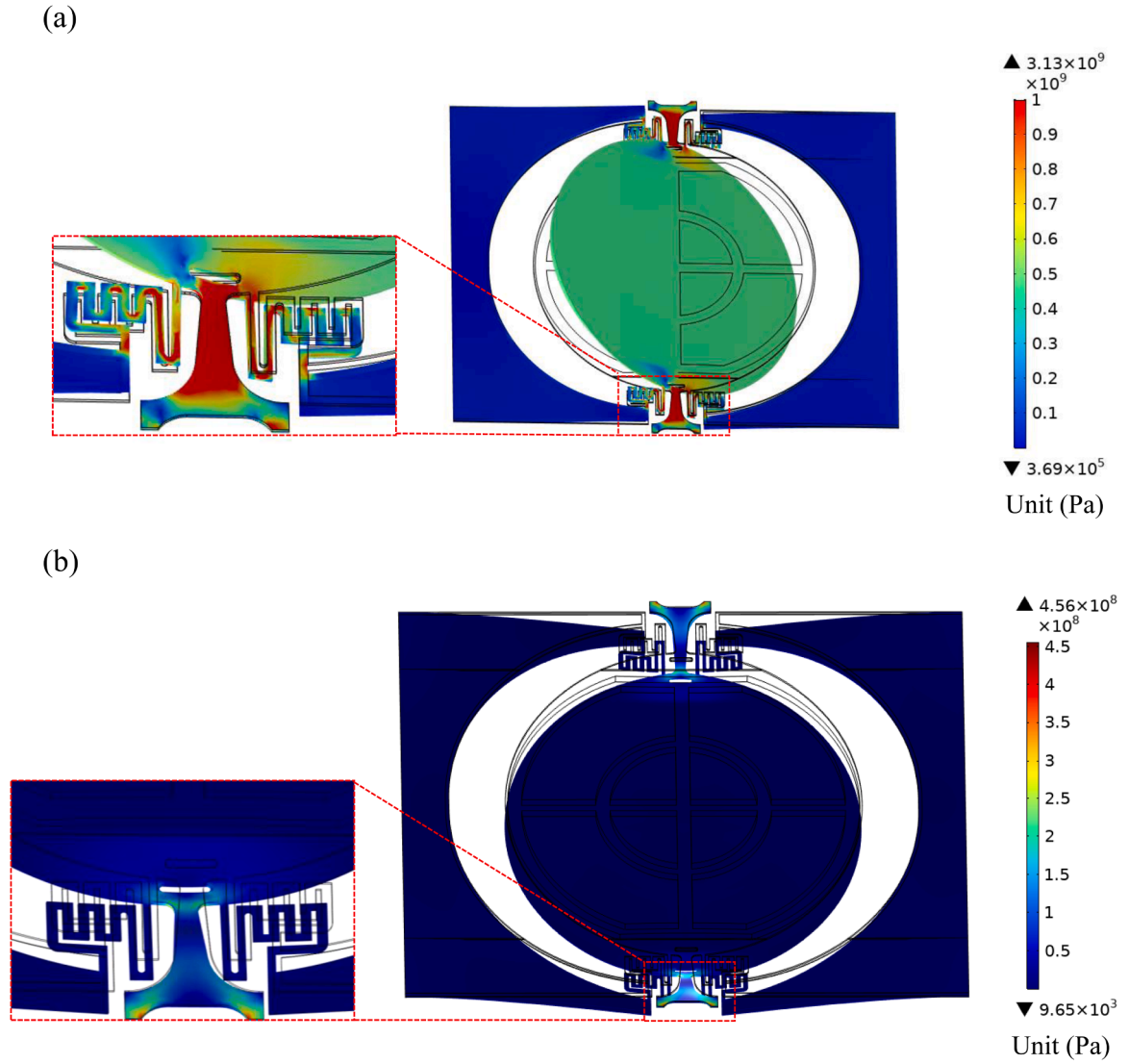


Fig. 4. The FEM simulations for von Mises stress distributions, (a) the stress distribution when the device is operating at 140-degree scan angle, and (b) the stress distribution when the device encounters a 1500 g shock. The unit of color bar is Pa.

could be express as,

$$U_{\sigma} = \int_0^L \frac{1}{2} \frac{(\frac{x}{L} w t_p \sigma Z_m)^2}{\frac{x}{L} (EI)_{eff}} dx \quad (5)$$

where t_p is the thickness of piezoelectric thin film, and $(EI)_{eff}$ is the equivalent moment of inertia of the actuator; and this strain energy can also be represented by the equivalent moment M_y of the residual stress,

$$U_{\sigma} = \int_0^L \frac{1}{2} \frac{(M_{\sigma})^2}{\frac{x}{L} (EI)_{eff}} dx \quad (6)$$

Since the strain energies U_{σ} and U_m are identical, M_{σ} can be deduced from Eqs. (5,6) as,

$$M_{\sigma} = \frac{(w t_p \sigma Z_m)^2}{2 \ln(L)} \quad (7)$$

After that, the Castigliano's theorem is applied to evaluate the static displacements of δ_z and θ_y through the actuator. In this regard, the strain energy of the actuator could be found as,

$$U = \int_0^L \frac{1}{2} \frac{(F \bullet x + M)^2}{\frac{x}{L} (EI)_{eff}} dx \quad (8)$$

where the total forces F and moments M on the actuator are respectively, $F = F_s + F_p$, and $M = M_s + M_{\sigma}$. According to the Castigliano's theorem [39], the linear tip displacement δ_z and angular tip displacement θ_y could be expressed as,

$$\delta_z = \frac{\partial U}{\partial F} = \frac{F \bullet L^3}{2(EI)_{eff}} + \frac{M \bullet L^2}{(EI)_{eff}} \quad (9)$$

$$\theta_y = \frac{\partial U}{\partial M} = \frac{L \bullet M \bullet \ln(L)}{2(EI)_{eff}} + \frac{F \bullet L^2}{(EI)_{eff}} \quad (10)$$

Substituting Eqs. (3), (4), (7) into the simultaneous Eqs. (9,10), the static displacement can be found as,

$$\begin{aligned} \delta_{SA} &= \delta_z \\ &= \left(\frac{L}{EI} \right) \left[(e_{31} V \frac{w}{L} Z_m) \left(\frac{L^2}{2} + \frac{C_1 L^2 (\ln(L)-2)}{2} \right) - \frac{(w t_p \sigma Z_m)^2}{2 \ln(L)} (L + w \frac{(2 \ln(L)-1)}{2} + C_3 \frac{3L^2}{2}) \right] \\ &= \left(\frac{L}{L * (\ln(L) - 4) (C_0 C_1 L + C_2 C_2 L) + 4 C_2 L + C_2 L^2 + C_1 \ln(L) + 1} \right) \end{aligned} \quad (11)$$

where

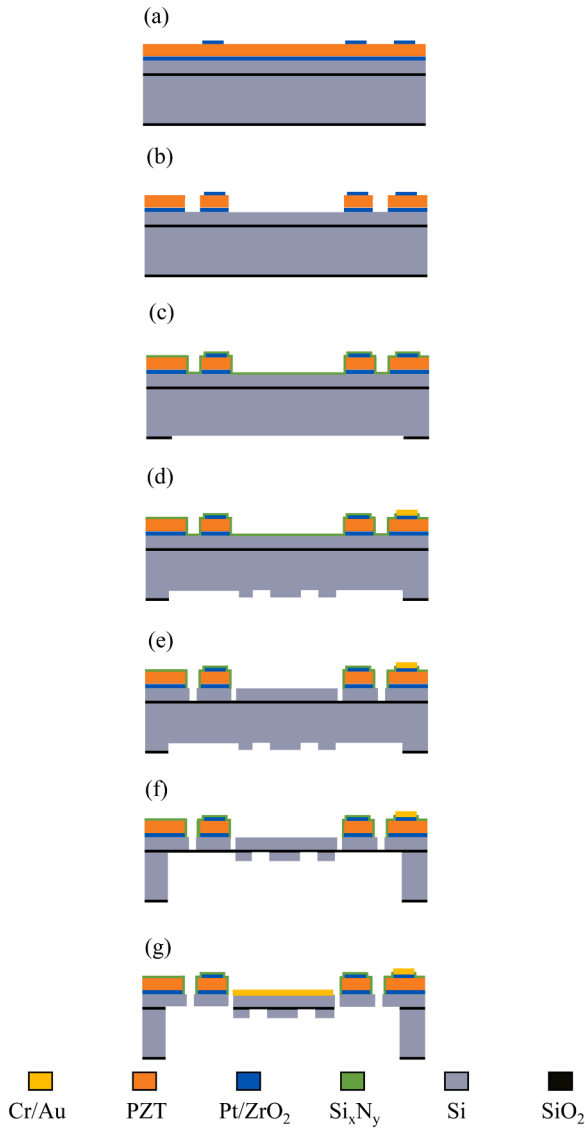


Fig. 5. Fabrication process steps.

$$C_0 = \frac{k_{zz} \cdot L}{2(EI)_{eff}}, \quad C_1 = \frac{k_{tt} \cdot L}{2(EI)_{eff}}, \quad C_2 = \frac{k_{tz} \cdot L}{2(EI)_{eff}}, \quad C_3 = \frac{k_{zt} \cdot L}{2(EI)_{eff}} \quad (12)$$

If the residual stress is negligible then Eq. (11) can be simplified as,

$$\delta_{SA} = \delta_z = \frac{L^3}{2EI} f(k_{zz}, k_{zt}, k_{tz}, k_{tt}) \left(e_{31} V \frac{w}{L} Z_m \right) \quad (13)$$

where

$$f(k_{zz}, k_{zt}, k_{tz}, k_{tt}) = \left(\frac{\frac{1}{2} + \frac{\ln(L)-2}{2}}{L * (\ln(L) - 4)(C_0 C_1 L + C_2 C_2 L) + 4C_2 L + C_2 L^2 + C_1 \ln(L) + 1} \right) \quad (14)$$

Finally, the Eq. (1) used to predict the dynamic displacement of mirror can be rewritten as,

$$\delta_{MD} = \frac{L^3}{2EI} f(k_{zz}, k_{zt}, k_{tz}, k_{tt}) \left(e_{31} V \frac{w}{L} Z_m \right) (QF)(TR) \quad (15)$$

As depicted in Eq. (15), the first term is the compliance of the actuator; the second term is mainly determined by the stiffness matrix of transmission spring (in Eq. (3)); the third term is the equivalent piezoelectric force; the fourth term is the quality factor of the actuator, and the last term is the transmission ratio. These terms show the design guideline to improve the scan angle. In addition to the straightforward approach to enhance the scan angle by using the piezoelectric thin film with higher e_{31} or increasing the driving voltage V , this study will focus on the design of transmission spring to increase the $f(k_{zz}, k_{zt}, k_{tz}, k_{tt})$. Based on Eq. (15), this study shows the transmission spring design on the proposed scanning mirror in Fig. 1. In comparison, the schematic illustrations in Table 1 show three scanning mirrors with the proposed and two reference transmission spring designs. The stiffness terms for these three spring designs are available in Table 2. Analytical solution suggests that the δ_{SA} of proposed design is 11.32 μm under 10 V driving. Comparing with the straight transmission spring design in A, the U-shape transmission spring could reduce the k_{zz} and k_{tt} by 73% and 28% respectively, so as to increase the displacement δ_{SA} for 85%. In addition, the proposed meandering transmission spring design could further reduce the k_{zz} and k_{tt} by 75% and 80%, this lead to a near two-fold improvement on δ_{SA} . The analytical results in Table 1 are also confirmed by the finite element method (FEM) simulations (by using the commercial FEM software COMSOL Multiphysics). Analytical results show good agreement with FEM simulations. In summary, based on the design guideline arrived from the analytical model in Eq. (15), this study presented the meandering transmission spring design to reduce its k_{zz} and k_{tt} and further increase the dynamic displacement δ_{DM} as well as the scan angle of the mirror plate.

2.2. FEM simulations

After soliciting the transmission spring designs using Eq. (15), the FEM simulations are employed to determine the stress distribution on springs to prevent failure under ultra-wide scan angle. Simulation results in Table 1 reveal that the proposed meandering spring design could reduce the stress. The FEM simulations are also employed to predict the dynamic responses of the designs. Fig. 3a shows the typical finite element model established in this study. Simulation results in Fig. 3b-d respectively depict the first three resonant frequencies and their corresponding mode shapes of the scanning mirror. Based on the design in this study, the scanning mirror is operating at its first resonant frequency at 1493 Hz with a torsional vibration mode, as indicated in Fig. 3b. Simulation shows that the 2nd mode (mirror plate having the out-of-plane linear motion) at 3984 Hz is far enough to avoid the cross talk with the operation mode, as depicted in Fig. 3c. Moreover, the 3rd mode in Fig. 3d features the rocking motion of the device at 8629 Hz.

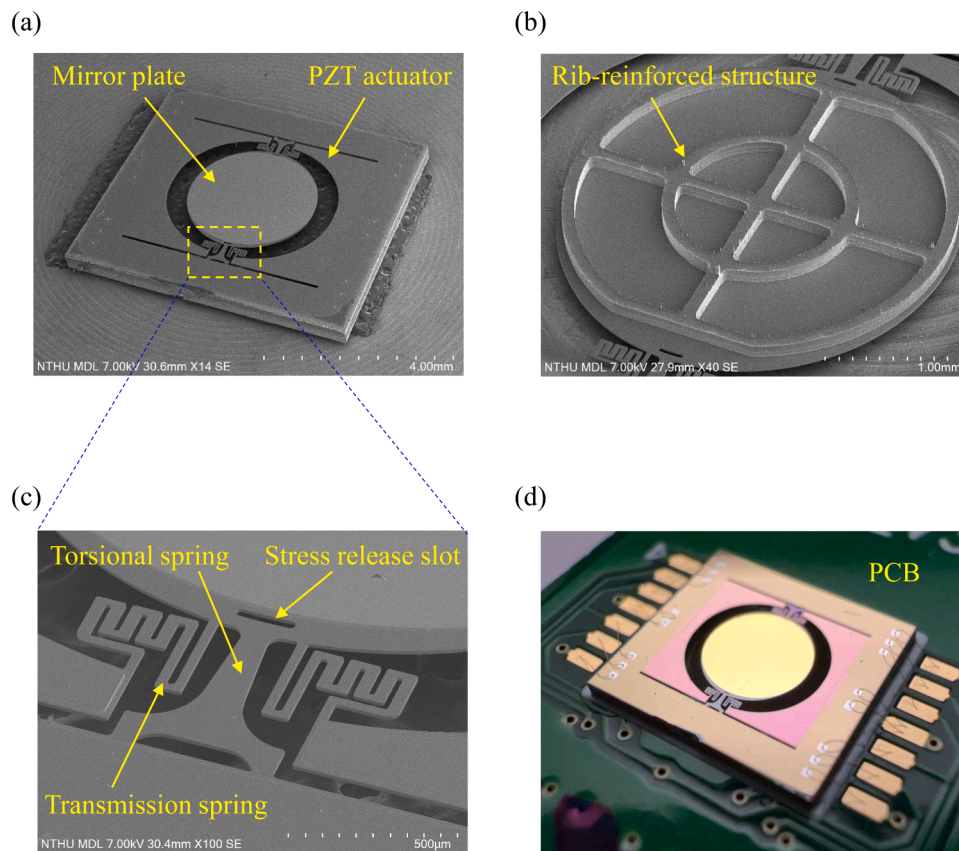


Fig. 6. The scanning electron microscope (SEM) micrographs of typical fabricated piezoelectric MEMS scanning mirror, (a) overview of the proposed design, (b) the backside view to show the rib reinforcement structure, and (c) the zoom-in micrograph of transmission springs and T-shape torsional spring; and the optical micrograph of (d) the scanning mirror wire bonded on the PCB ready for testing.

The FEM simulations are also used for stress analysis of the scanning mirror during operation. Fig. 4a demonstrates stress distributions (von Mises stress with unit in Pa) on the scanning mirror when operating at 140-degree optical scan angle. Simulations indicate higher stresses are distributed at the torsional spring and the transmission spring, especially near the connections with the mirror plate. As shown in Table 1, the proposed meandering transmission spring design could lower its stress, yet still have a large scan angle. Moreover, the slots on the mirror plate could provide additional compliance to reduce the stress on torsional spring. Simulations indicate the maximum stress of the mirror at a 140-degree optical scan angle was 3.13 GPa. It is worth to note that the slot will induce a large stress when device is under shock loading. Simulation results in Fig. 4b show the stress distribution (von Mises stress with unit in Pa) of the proposed scanning mirror when encounter a 1500 g shock loading. The maximum stress occurs at the edge of the slot with a value of 456 MPa which is much smaller than the yield strength of silicon.

3. Fabrication and results

Fig. 5 displays the fabrication steps to implement the proposed scanning mirrors. In this study, the 10-mask micromachining processes were performed on the SOI (silicon-on-insulator) substrate with a 15 μm thick device layer. As shown in Fig. 5a, the Pt and ZrO_2 films were deposited on the substrate to serve as the bottom electrode and adhesion layer, and then the 5 μm thick PZT film was sputtered on the bottom electrode. After that, the Pt film was deposited and then patterned by the lift-off process to act as the top electrode. As depicted in Fig. 5b, the PZT thin film was patterned by the ion milling process. The bottom Pt electrode was then patterned by using the RIE (reactive ion etching) process.

Moreover, as indicated in Fig. 5c, a thin Si_3N_4 film was deposited by PECVD as the passivation layer to protect the PZT film from environmental moisture. After that, the backside oxide layer was etched by the RIE to define the cavity region. As displayed in Fig. 5d, backside deep-RIE processes on the Si substrate were performed to define pattern and thickness of mirror ribs. After that, the Si_3N_4 passivation layer was patterned by the RIE to expose the contact area of top electrode and metal film was deposited and then patterned by the lift-off process to define the bonding pads. As exhibited in Fig. 5e, the Si_3N_4 passivation layer was again patterned by the RIE to expose reflection area, and then the front-side deep-RIE etching process on the device Si layer was employed to define the shape of scanner (such as the spring, mirror plate, etc.). The second backside deep-RIE was performed to etch the remaining Si handle layer, illustrated in Fig. 5f. Finally, the reflection metal layer was deposited on the mirror plate by using the shadow mask, then the buried oxide was etched to release the structure, shown in Fig. 5g.

Typical fabrication results are shown in Fig. 6. The SEM (scanning electron microscope) micrographs in Fig. 6a-b respectively display the front side and backside of a typical fabricated chip which containing the proposed scanning mirror. The rib-reinforced structures are observed through the backside cavity of the chip. The zoom-in SEM micrograph in Fig. 6c exhibits the proposed meandering transmission springs with both ends respectively connected to the piezoelectric actuators and the mirror plate; and the T-shape torsional spring with both ends respectively connected to the mirror plate and the substrate. The slot on mirror plate for stress release is also observed. The micrograph in Fig. 6d shows the chip with micro scanner is fixed and wire-bonded on the printed circuit board (PCB) for testing. This study characterized the shape of the

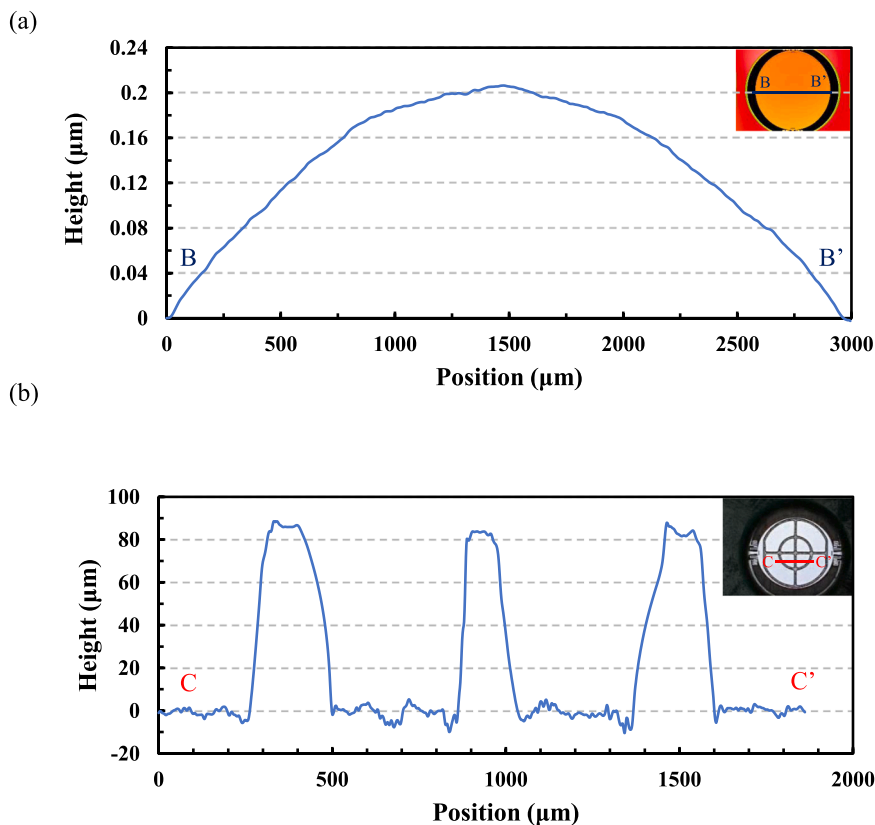


Fig. 7. (a) Initial bending of the mirror plate (radius of curvature of the mirror plate is 5.6 m) measured using the optical interferometer, and (b) the thickness of rib structure (thickness is around 80 μm) measured using the laser confocal microscope from the backside of the chip.

fabricated scanning mirror before performance tests. According to measurements from the commercial optical interferometer, as depicted in Fig. 7a, the bending radius of curvature of the mirror plate is 5.03 m, and this value could fulfill the optical requirements [40]. The results show that the proposed mirror plate design has sufficient stiffness to suppress the influence of thin film residual stresses. This study also employs the laser confocal microscope to measure the thickness of the rib. As shown in Fig. 7b, the thickness of ribs is near 84 μm , which is close to the original design value of 80 μm .

4. Measurements and discussions

This study performed various tests to evaluate the performances of the fabricated scanning mirrors. The micrograph in Fig. 8a display the micro scanning mirror with no input voltage. The micrograph in Fig. 8b further exhibits the micro scanning mirror driving at its resonant frequency. The blurred pattern of the mirror plate depicts its mechanical scan angle. The commercial Laser Doppler Vibrometer (LDV, Polytec GmbH) and Digital Holographic Microscope (DHM, Lyncee Tec) are employed to measure the dynamic characteristics of the scanning mirrors. Results in Fig. 9a show typical frequency responses of the scanning mirror (under 15 kHz frequency sweeping) measured by the LDV, and three resonant frequencies are detected within the frequency range. Moreover, as displayed in Fig. 9b, typical measurement results from the DHM (see the supplementary information in Video 1 and Video 2) are used to observe the corresponding mode shapes for each resonant frequency. According to the results from LDV and DHM, the 1st resonant

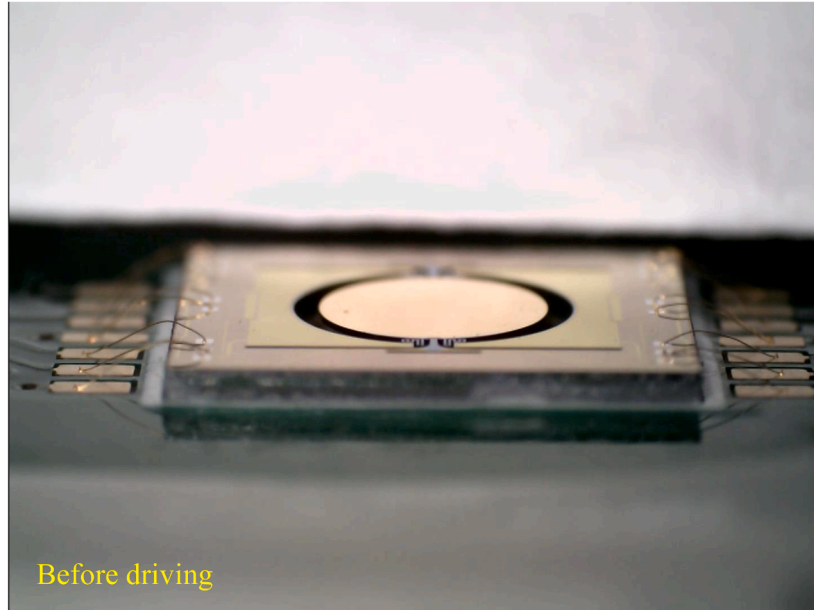
frequency of the scanning mirror is 1502 Hz with the quality factor of near 440, and the vibration mode is featuring with the tilting oscillation of mirror plate. Measured 1st resonant frequency shows good agreement with simulation result. As shown in Fig. 10a, the experiment setup was established to measure the optical scan angle of the micro scanner. The actuating U-shape cantilever was driven by the function generator and power amplifier. A laser beam was incident on the scanning mirror and then projected on a fixed circular screen. The optical scan angle can be directly measured from the attached protractor. The left photo in Fig. 10b shows the typical scanning pattern during the test. The chip with micro scanner can be observed in the right top zoom-in photo of Fig. 10b. Moreover, as display in the right below photo, the optical scan angle is measured from the protractor.

Supplementary material related to this article can be found online at [doi:10.1016/j.sna.2022.114010](https://doi.org/10.1016/j.sna.2022.114010).

Supplementary material related to this article can be found online at [doi:10.1016/j.sna.2022.114010](https://doi.org/10.1016/j.sna.2022.114010).

Measurement results in Fig. 11 exhibit the frequency responses of the proposed scanning mirror under four different driving voltages (5 V ~ 30 V). The results indicate the scan angle of the mirror is increased with the driving voltage. Meanwhile, the frequency response curves would bend toward high frequency for higher driving voltage and the nonlinear jumping phenomenon is also observed. The large scan angle may lead the spring hardening effect and further cause the nonlinear dynamic responses of the mirror [32,41,42]. Thus, the feedback control of scanning mirror is imperative to achieve large scan angle while preventing operation falling into nonlinear jump. Measurements in Fig. 12a exhibit

(a)



(b)

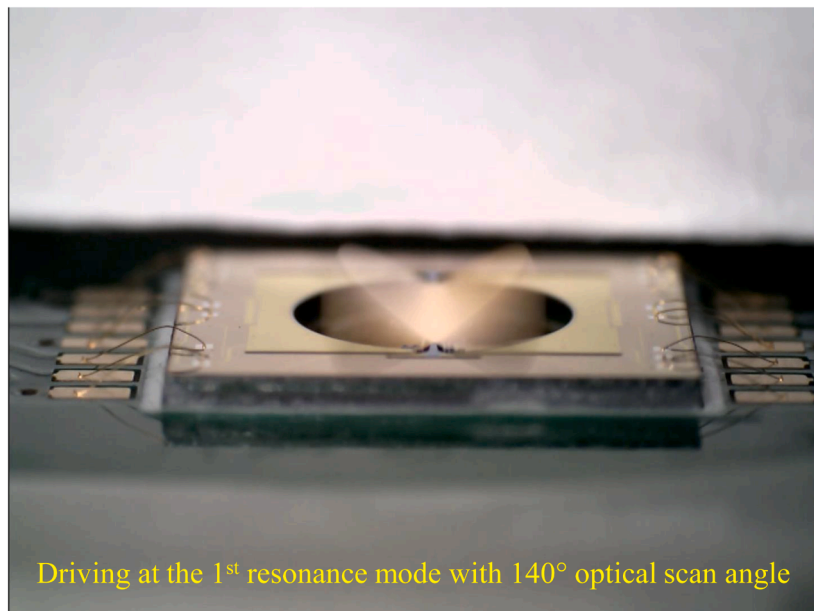
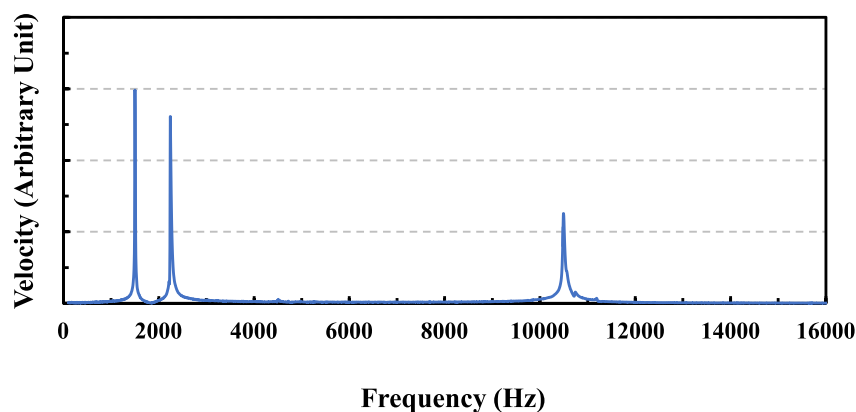
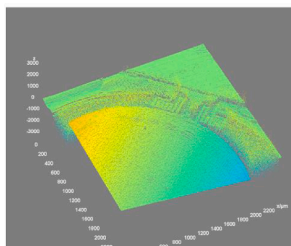


Fig. 8. Optical micrographs to show the presented scanning mirror, (a) before driving, and (b) driving with a 140-degree optical scan angle, the mechanical scan angle can be observed from the blur image of the mirror plate.

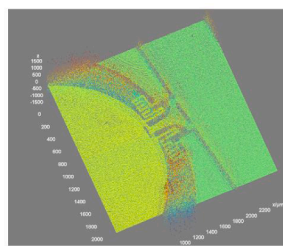
(a)



(b)



1st resonant mode:
mirror plate having torsional
vibration



2nd resonant mode:
mirror plate having out-of-
plane linear vibration

Fig. 9. (a) The frequency responses of the presented scanning mirror measured using the laser Doppler vibrometer, and the first three resonant frequencies were found under 15 kHz; (b) the 3D motion images of the presented scanning mirror measured using the digital holographic microscope; the left and right images captured from the 3D motion images (Video 1 and Video 2 of the supplementary information) respectively display the scanning mirror driven at the tilting mode (the 1st resonant frequency) and the piston mode frequency (the 2nd resonant frequency).

the optical scan angle varying with the driving voltage. The results indicate the proposed scanning mirror can reach an extremely large optical scan angle of 140-degree under a unipolar driving voltage of 42 V. It is worth to note that the above scan angle was achieved for scanners with no vacuum packaging. The results show the presented design determined from the analytical model could improve the scan angle of mirror. Measurements in Fig. 13 further depict the relationship between the optical scan angle and the signal detected by the PZT film on the U-shape sensing cantilever. The sensing signals show good linearity with the scan angles and can be exploited as the feedback control. In short, one of the U-shape cantilevers acts as the actuator to drive the mirror by inverse piezoelectric effect, and the other U-shape cantilever picks up sensing signals by direct piezoelectric effect.

In this study, the PZT layer is protected by the silicon nitride film from harsh environment. To verify the reliability of the device, the micro scanner was tested in high humidity chamber (95%RH, room temperature) under 10 V_{pp} resonant driving for 7 days (equivalent to roughly 0.2 billion cycles). Measurements in Fig. 14 indicate that the deviation of scan angle is less than 10% after the driving tests in harsh environment. Finally, based on the standard MIL-STD-883 G TM 2002.4 Condition B [43], this study also performed the shock tests with 1500 g loading in six different directions (+/- X, +/- Y, +/- Z) on the micro scanner. The peak duration of shock was 0.5 ms, and totally 5 shocks in each direction. Test

conditions were summarized in Table 4 and frequency responses of the scanner under 15 V_{pp} driving before and after shock were displayed in Fig. 15. It indicates the frequency responses of the micro scanner have minor changes after shock tests (only 7 Hz difference in resonant frequency). Moreover, no damages were observed on the micro scanner after shock tests. The results indicate that the micro scanner could withstand 1500 g shock loading. The temperature stability of the device has also been studied. The scanning mirror was tested in an oven to control the ambient temperature (ranging from -20 °C to 80 °C). It is not straightforward to perform the optical measurement in Fig. 10 inside the oven. In this study, based on the calibration curve in Fig. 13, the scan angle (at different ambient temperature) is determined from the signal measured by the U-shape PZT sensor. Typical measurement results shown in Fig. 16 indicate the dynamic responses of the device remain consistence as ambient temperature varying from -20–40 °C. However, as the ambient temperature increasing to 60 °C or above, the dynamic responses of the scanning mirror are changed, particularly at and after the resonant peak. Further investigations are required to explain the measurement results.

The comparison of the analytical, simulated, and experimental results is shown in Fig. 12b and Table 3. The d_{31} coefficient was extracted using suspended cantilever testkey. Analytical and experimental results have good agreement under small driving voltage (under 10 V), errors

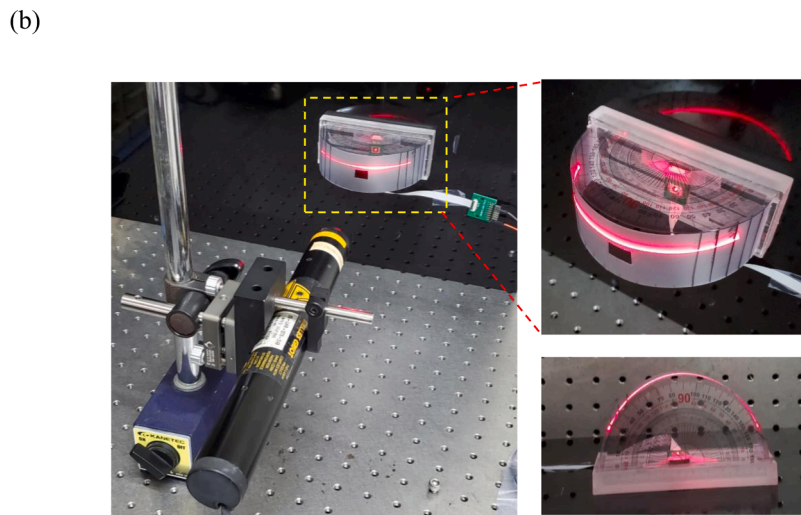
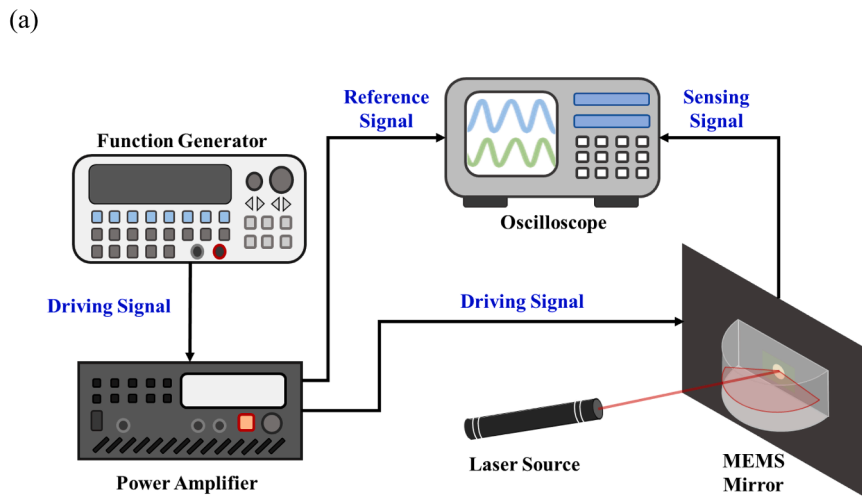


Fig. 10. (a) Schematic illustration of the experiment setup to measure the optical scan angle. (b) The left micrograph displays part of the test setup. The zoom-in micrographs show the laser scan pattern projected on the circular screen, and the scan angle can be measured by the protractor.

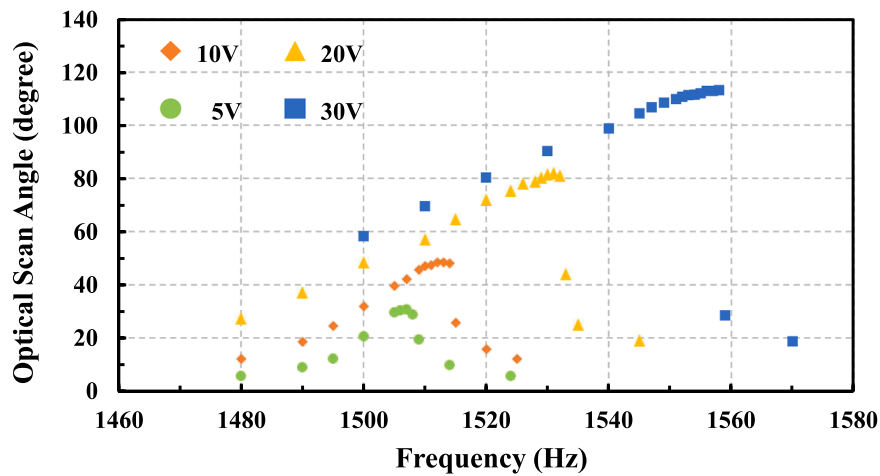


Fig. 11. Measured frequency responses of the proposed scanning mirror under four different driving voltages (5 V ~ 30 V).

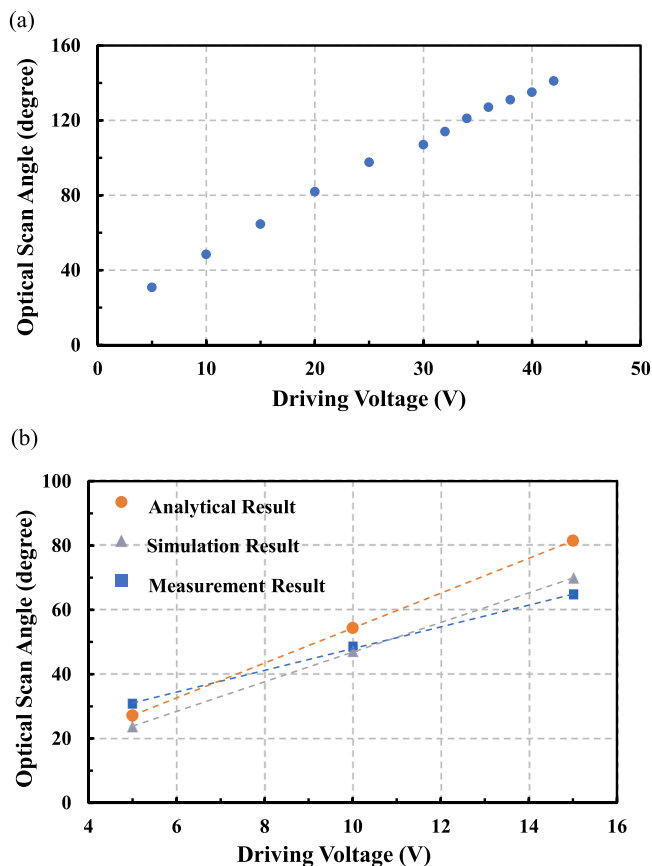


Fig. 12. (a) Measurements to show the variation of optical scan angle with the driving voltage, and (b) comparison between measurement, analytical, and simulation results at small driving voltage range.

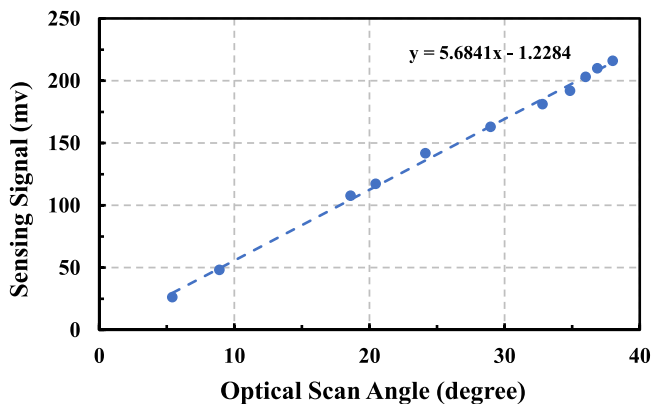


Fig. 13. Variation of measured sensing signals (from the U-shape piezoelectric sensor) with mechanical scan angles.

between these results were within 10%, showing the feasibility of using analytical model to simplify the design process. As the driving voltage rises, the error between analytical solutions and measurement results increases accordingly. The spring hardening effect discussed in Fig. 11 was considered as the reason to cause the error between the analysis and measurement at higher driving voltage. Thus, the scanning angle per driving voltage predicted by the analytical model has higher value.

5. Conclusions

This study presents the design and implementation of a piezoelectric scanning mirror with large reflection area and wide scan angle for vehicle LiDAR applications. The mirror plate is supported by two T-shape torsional springs which anchored to the substrate. Two U-shape silicon cantilevers covered with unimorph PZT film are respectively

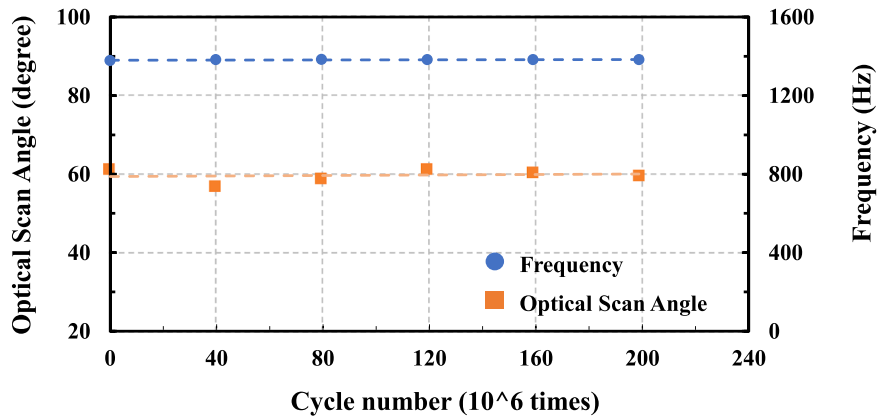


Fig. 14. Deviation of the optical scan angle and the scanning frequency during the cycling tests under the high humidity environment.

Table 3

Summary of the parameters used in analysis and simulation, and the comparison of the analysis, simulation, and measurement results.

	Analytical	Simulation	Measurement
Si Young's modulus (GPa)	169		
Si shear modulus(GPa)	60		
PZT Young's modulus (GPa)	61		
d ₃₁ coefficient (pm/V)	160		
Quality factor	440		
1 st Resonant Frequency (Hz)		1493	1502
2 nd Resonant Frequency (Hz)		3984	2563
Angle per voltage (°/V)	5.43	4.61	3.38

Table 4

Conditions for the shock test.

	Shock Test Conditions
Pulse form	Half sine
Acceleration (g)	1500 ± 20%
Peak duration (ms)	0.5 ± 30%
Number of shock	5 shocks per direction
Shock direction	(+/- X, +/- Y, +/- Z)
Total shocks	30

used as the actuator and sensor to drive the mirror plate and also detect its scan angle. The U-shape actuator excites the mirror plate through the transmission springs. Thus, the transmission spring plays an important role to determine the scan angle of mirror plate. In this regard, this study has established the analytical model to evaluate and decide the design of transmission springs. Moreover, the FEM simulations are used to predict the dynamic characteristics and stress distribution of the scanning mirror. Based on the design guideline arrived from the analytical model, this study presented the meandering transmission spring design to increase the dynamic displacement as well as the scan angle of a large mirror plate. The processes on the SOI wafer with the PZT film were developed to fabricate the presented scanning mirrors. Measurements show the mirror has a maximum optical scan angle of 140-degree when driving at its resonant frequency of 1.5 kHz with a unipolar driving voltage of 42 V. Since the test is under 1 atm ambient pressure, the optical scan angle is extremely large for the MEMS scanner with a mirror plate of 3 mm in diameter. The sensing signals detected by the U-shape piezoelectric sensor show good linearity with the scan angles of mirror plate. The sensor can be exploited as the feedback control for future applications. Note that the U-shape piezoelectric sensor can be exploited to drive the mirror plate to reduce the driving voltage if feedback sensing signals are not required (or can be provided by other position sensor [44,45]). The reliability tests show that the micro scanner could withstand 1500 g shock loading. In addition, the deviation of scan angle is less than 10% after the cycling test under 10 V_{pp} resonant driving in 95%RH and room temperature for 0.2 billion cycles. The analytical

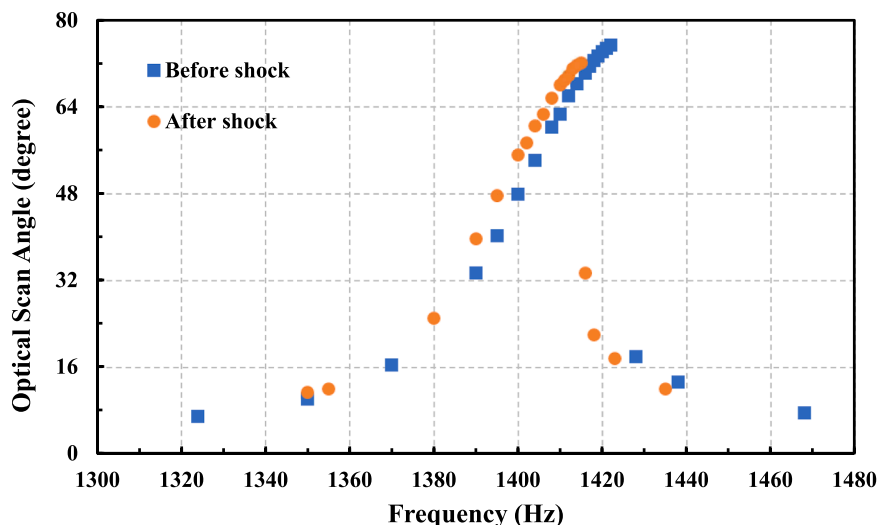


Fig. 15. Frequency responses of the micro scanner before and after shock test.

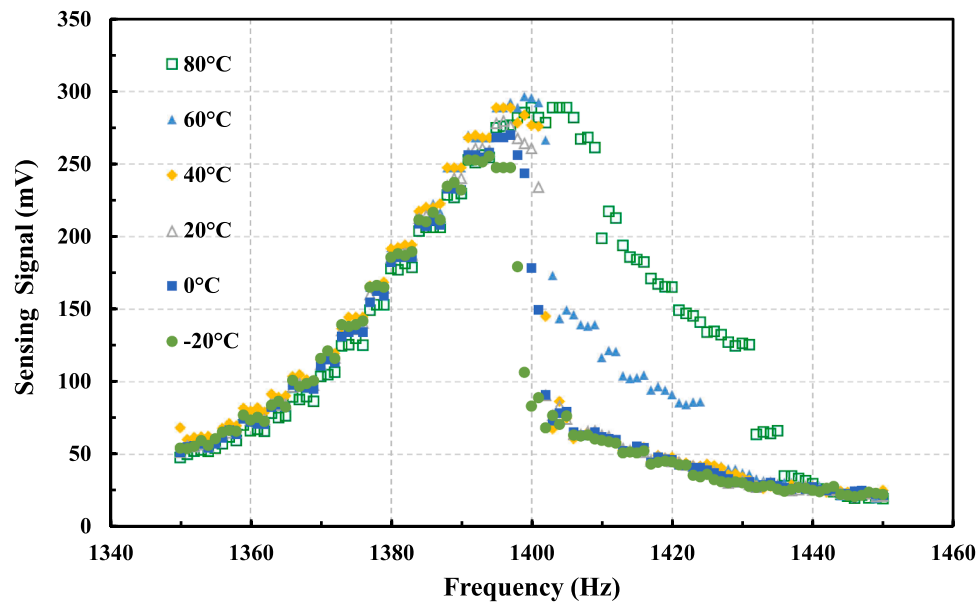


Fig. 16. Frequency responses measured at different temperatures (ranging from -20°C to 80°C).

results have good agreement with FEM simulations and measurements. Thus, the analytical model established in this study offer a simple guideline to design the transmission spring of the scanning mirror. The ad-hoc approach to design the scanning mirror can be avoided. After that, the FEM simulations could further provide more detail information about the performances of scanning mirror. Nevertheless, at higher driving voltage, nonlinear effect starts to become more pronounce, error between analysis and measurement results thus increased. To make a correction of the error, the nonlinear terms can be added into the stiffness matrix of analytical model, so that the stiffness terms become displacement dependent [46].

Declaration of Competing Interest

The authors declare the following financial interests/personal relationships which may be considered as potential competing interests: Weileun Fang reports financial support and administrative support were provided by ministry of science and technology of Taiwan.

Data Availability

The authors are unable or have chosen not to specify which data has been used.

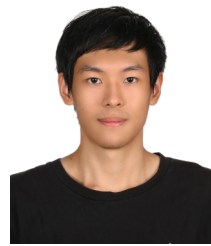
Acknowledgements

This project was supported by the National Science and Technology Council of Taiwan under the grant number MOST 110-2218-E-007-032, NSTC 111-2221-E-007-070-MY3 and NSTC 111-2221-E-007-069-MY3. The authors would like to thank Coretronic MEMS Corporation for their help with device fabrication, and packaging.

References

- [1] U. Hofmann, F. Senger, F. Soerensen, V. Stenchly, B. Jensen, and J. Janes, Biaxial resonant 7mm-MEMS mirror for automotive LIDAR application, *International Conference on Optical MEMS and Nanophotonics*, Banff, Canada, August 2012, pp. 150–151.
- [2] Y.-C. Ko, J.-W. Cho, Y.-K. Mun, H.-G. Jeong, W.K. Choi, J.-W. Kim, Eye-type scanning mirror with dual vertical combs for laser display, *Sens. Actuators A: Phys.* vol. 126 (1) (2006) 218–226.
- [3] C. Liao, J. Tsai, The evolution of MEMS displays, *IEEE Trans. Ind. Electron.* vol. 56 (4) (2009) 1057–1065.
- [4] W.O. Davis, R. Sprague, and J. Miller, "MEMS-based pico projector display," in *2008 IEEE/LEOS International Conference on Optical MEMS and Nanophotonics*, Freiburg, Germany, August 2008, pp. 31–32.
- [5] D. Dana, M.D. Walter, and S. John, "Emerging digital micromirror device (DMD) applications," *MOEMS display and imaging systems*, San Jose, CA, January 2003, pp. 14–25.
- [6] G.A. Feather and D.W. Monk, "The digital micromirror device for projection display," in *Proceedings IEEE International Conference on Wafer Scale Integration*, San Francisco, CA, January 1995, pp. 489–493.
- [7] A.C.L. Hung, H.Y.H. Lai, T.-W. Lin, S.-G. Fu, M.S.C. Lu, An electrostatically driven 2D micro-scanning mirror with capacitive sensing for projection display, *Sens. Actuators A Phys.* vol. 222 (2015) 122–129.
- [8] Y. An, B. Sun, P. Wang, L. Xiao, H. Liu, H. Xie, A 1×20 MEMS mirror array with large scan angle and low driving voltage for optical wavelength-selective switches, *Sens. Actuators A: Phys.* vol. 324 (2021), 112689.
- [9] T. Liu, T. Pan, P. Wang, S. Qin, H. Xie, Scanning optimization of an electrothermally-actuated MEMS mirror for applications in optical coherence tomography endoscopy, *Sens. Actuators A: Phys.* vol. 335 (2022), 113377.
- [10] B. Jiang, M. Peng, Y. Liu, T. Zhou, Y. Su, The fabrication of 2D micromirror with large electromagnetic driving forces, *Sens. Actuators A Phys.* vol. 286 (2019) 163–168.
- [11] F. Schwarz, F. Senger, J. Albers, P. Malaurie, C. Janicke, and L. Pohl, "Resonant 1D MEMS mirror with a total optical scan angle of 180° for automotive LiDAR," *MOEMS and Miniaturized Systems XIX*, Santa Clara, CA, February 2020, Vol. 11293, p. 1129309.
- [12] J.-H. Lee, Y.-C. Ko, H.-M. Jeong, B.-S. Choi, J.-M. Kim, D.Y. Jeon, SOI-based fabrication processes of the scanning mirror having vertical comb fingers, *Sens. Actuators A: Phys.* vol. 102 (1) (2002) 11–18.
- [13] M. Wu, H.Y. Lin, W. Fang, A poly-Si-based vertical comb-drive two-axis gimbaled scanner for optical applications, *IEEE Photonics Technol. Lett.* vol. 18 (20) (2006) 2111–2113.
- [14] J.-W. Cho, Y.-H. Park, Y.-C. Ko, B.-L. Lee, S.-J. Kang and S.-W. Chung, "Electrostatic 1D microscanner with vertical combs for HD resolution display," *MOEMS and Miniaturized Systems VI*, Santa Clara, CA, January 2007, Vol. 6466, pp. 106–117.
- [15] H. Schenk, P. Dürr, D. Kunze, H. Lakner, H. Kück, A resonantly excited 2D-micro-scanning-mirror with large deflection, *Sens. Actuators A Phys.* vol. 89 (1) (2001) 104–111.
- [16] D.M. Tanner, J.A. Walraven, K. Helgesen, L.W. Irwin, F. Brown, and N.F. Smith, "MEMS reliability in shock environments," *IEEE International Reliability Physics Symposium Proceeding*, San Jose, CA, April 2000, pp. 129–138.
- [17] S.-H. Chung, S.-K. Lee, C.-H. Ji, J.-H. Park, Vacuum packaged electromagnetic 2D scanning micromirror, *Sens. Actuators A Phys.* vol. 290 (2019) 147–155.
- [18] H. Yang, T. Tang, S.T. Lee, W. Fang, A novel coilless scanning mirror using eddy current lorentz force and magnetostatic force, *J. Micro Syst.* vol. 16 (3) (2007) 511–520.
- [19] A.D. Yalcinkaya, H. Urey, D. Brown, T. Montague, R. Sprague, Two-axis electromagnetic microscanner for high resolution displays, *J. Micro Syst.* vol. 15 (4) (2006) 786–794.

- [20] Y.-H. Chang, G. Hao, C.-S. Liu, Design and characterisation of a compact 4-degree-of-freedom fast steering mirror system based on double Porro prisms for laser beam stabilization, *Sens. Actuators A Phys.* vol. 322 (2021), 112639.
- [21] S.T.S. Holmström, U. Baran, H. Urey, MEMS laser scanners: a review, *J. Micro Syst. vol.* 23 (2) (2014) 259–275.
- [22] (a) C. Zinck, D. Pinceau, E. Defay, E. Delevoe, D. Barbier, Development and characterization of membranes actuated by a PZT thin film for MEMS applications, *Sens. Actuators A Phys.* vol. 115 (2) (2004) 483–489;
(b) T. Masanao, M. Akamatsu, Y. Yasuda, H. Fujita, and H. Toshiyoshi, "A Combination of Fast Resonant Mode and Slow Static Deflection of SOI-PZT Actuators for MEMS Image Projection Display," *IEEE/LEOS International Conference on Optical MEMS and Their Applications Conference*, Big Sky, MT, August 2006, pp. 25–26.
- [23] A. Piot, J. Pribošek, and M. Moridi, "Dual-Axis Resonant Scanning MEMS Mirror with Pulsed-Laser-Deposited Barium-Doped PZT," *IEEE MEMS Conference*, Gainesville, FL, January 2021, pp. 89–92.
- [24] N. Boni, R. Carminati, G. Mendicino, and M. Merli, "Quasi-static PZT actuated MEMS mirror with 4×3mm² reflective area and high robustness," *MOEMS and Miniaturized Systems XX*, Santa Clara, CA, March 2021, Vol. 11697, pp. 1169708.
- [25] A. Piot, J. Pribošek, J. Maufay, J. Schicker, A. Tortschanoff, and R. Matloub, "Resonant PZT MEMS Mirror with Segmented Electrodes," *IEEE MEMS Conference*, Vancouver, Canada, January 2022, pp. 517–520.
- [26] X.-H. Xu, Y. Feng, B.-Q. Li, J.-R. Chu, Integration of displacement sensor into bulk PZT thick film actuator for MEMS deformable mirror, *Sens. Actuators A: Phys.* vol. 147 (1) (2008) 242–247.
- [27] H.W. Yoo, N. Druml, D. Brunner, C. Schwarzl, T. Thurner, and M. Hennecke, "MEMS-based lidar for autonomous driving," *e & i Elektrotechnik und Informationstechnik*, pp. 408–415, 2018.
- [28] A. Guy, R. Elan, S. Dadi, G. Nir, K. Sivan, and N. Sivan, "Multiple MEMS mirrors synchronization techniques, modeling, and applications," *MOEMS and Miniaturized Systems XX*, Santa Clara, CA, March 2021, vol. 11697, pp. 116970C.
- [29] Y. Zhu, W. Liu, K. Jia, W. Liao, H. Xie, A piezoelectric unimorph actuator based tip-tilt-piston micromirror with high fill factor and small tilt and lateral shift, *Sens. Actuators A Phys.* vol. 167 (2) (2011) 495–501.
- [30] T. Masanao, A. Masahiro, Y. Yoshiaki, and T. Hiroshi, "A two-axis piezoelectric tilting micromirror with a newly developed PZT-meandering actuator," *IEEE MEMS Conference*, Hyogo, Japan, January 2007, pp. 699–702.
- [31] U. Baran, D. Brown, S. Holmstrom, D. Balma, W.O. Davis, P. Muralt, Resonant PZT MEMS scanner for high-resolution displays, *J. Micro Syst. vol.* 21 (6) (2012) 1303–1310.
- [32] K. Meinel, C. Stoeckel, M. Melzer, S. Zimmermann, R. Forke, K. Hiller, Piezoelectric scanning micromirror with built-in sensors based on thin film aluminum nitride, *IEEE Sens. J.* vol. 21 (8) (2021) 9682–9689.
- [33] G. Mendicino, M. Merli, R. Carminati, N. Boni, A. Opreni, and A. Frangi, Electro-mechanical validation of a resonant MEMS mirror with PZT actuation and PZR sensing, *MOEMS and Miniaturized Systems XX*, Santa Clara, California, March 2021, vol. 11697, 1169715.
- [35] H.-Y. Lin, W. Fang, A rib-reinforced micro torsional mirror driven by electrostatic torque generators, *Sens. Actuators A: Phys.* vol. 105 (1) (2003) 1–9.
- [36] R. Farrugia, I. Grech, O. Casha, J. Micallef, and E. Gatt, "Analysis of dynamic deformation in 1-D resonating micromirrors," *Symposium on Design, Test, Integration and Packaging of MEMS/MOEMS*, Budapest, Hungary, May 2016, pp. 1–6.
- [37] D.J. Inman, R.C. Singh, *Engineering Vibration*, Prentice Hall, Englewood Cliffs, 1994.
- [38] H. Tiersten, Hamilton's principle for linear piezoelectric media, *Proc. IEEE* vol. 55 (8) (1967) 1523–1524.
- [39] J.H. Argyris, S. Kelsey, *Energy Theorems and Structural Analysis*, Springer, London, 1960.
- [40] H. Urey, D. Wine, and T. Osborne, "Optical performance requirements for MEMS-scanner based microdisplays," *MOEMS and Miniaturized Systems*, Santa Clara, CA, August 2000, pp. 176–185.
- [41] A. Frangi, A. Opreni, N. Boni, P. Fedeli, R. Carminati, M. Merli, Nonlinear response of PZT-actuated resonant micromirrors, *J. Micro Syst. vol.* 29 (6) (2020) 1421–1430.
- [42] P. Deng and W. Ma, "Nonlinearity investigation of the MEMS scanning mirror with electrostatic comb drive," *IEEE International Conference on Nano/Micro Engineered and Molecular Systems*, Hawaii, HI, April, 2014, pp. 212–215.
- [43] E. Higurashi, R. Sawada, T. Suga, Test method standard, microcircuits, method 2019.7 MIL-STD-883G, test method standard, microcircuits, method 2019.7, 2006, *IEICE Trans. Electron.* (2009) 231–238.
- [44] A. Vergara, T. Tsukamoto, W. Fang, S. Tanaka, Integration of buried piezoresistive sensors and PZT thin film for dynamic and static position sensing of MEMS actuator, *J. Micro Syst. vol.* 30 (11) (2020), 115020.
- [45] A. Vergara, T. Tsukamoto, W. Fang, S. Tanaka, Feedback control of thin film PZT MEMS actuator with integrated buried piezoresistors, *Sens. Actuators A Phys.* vol. 332 (2021), 113131.
- [46] A.H. Nayfeh, D.T. Mook, *Nonlinear Oscillations*, John Wiley & Sons, 2008.



Hao-Chien Cheng was born in Changhua, Taiwan. In 2020, he received his B.S. degree from the Department of Power Mechanical Engineering, National Tsing Hua University, Taiwan. In 2022, he received his M.S. degree from the Institute of NanoEngineering and MicroSystems, National Tsing Hua University, Taiwan. Since 2022, he works as research and development engineer at Coretronic MEMS Corporation. His current research interests include MEMS scanning mirror, thin film piezoelectric materials and reliability of MEMS devices.



Shi-Chi Liu was born in Miaoli, Taiwan. In 2020, he received his B.S. degree from the Interdisciplinary Program of Nuclear Science, National Tsing Hua University, Taiwan. In 2022, he received his M.S. degree from the Department of Power Mechanical Engineering, National Tsing Hua University, Taiwan. Since 2022, he works as research and development engineer at Taiwan Semiconductor Manufacturing Co., Ltd. His current research interests include MEMS scanning mirror design, piezoelectric actuator design, piezoelectric and mechanical properties of thin film piezoelectric materials.



Chih-Chen Hsu was born in Tainan, Taiwan. In 2021, she received her B.S. degree from the Department of Power Mechanical Engineering, National Tsing Hua University, Taiwan. She is currently a Master student in the Institute of NanoEngineering and MicroSystems, National Tsing Hua University, Taiwan. Her research interests include bi-axial MEMS scanning mirror design and characterization of thin film piezoelectric materials.



Hung-Yu Lin was born in Chiayi, Taiwan. He received his B.S. degree from the Department of Mechanical Engineering, National Central University, Taiwan. He is currently a Master student in the Department of Power Mechanical Engineering, National Tsing Hua University, Taiwan. His research interests include high frequency MEMS scanning mirror and scanning mirror applications in head-up display system.



Fuchi Shih was born in Taipei, Taiwan. He received the B.S. and M.S. degrees from the Automatic Control Engineering Department, Feng Chia University, Taichung, Taiwan, in 2018 and 2020, respectively. He is currently pursuing the Ph.D. degree in the Institute of NanoEngineering and MicroSystems, National Tsing Hua University, Taiwan. His research interests include MEMS devices, micro-probe with thermal sensor integration and the design of CMOS-MEMS tactile sensing hub.



Dr. Mingching Wu is working in Coretronic MEMS Corporation(CMC) as President. He has completely experiences in the front-end and back-end sensor industries, and also familiar with sensor manufacturing Eco-systems. Before joining CMC, He established GlobalMEMS in 2013 to develop and mass production various sensors such as G-sensor, P-sensor, and F-force. Moreover, he worked closely with Japanese company to develop next generation sensing technology. Dr. Wu has accumulated 20 years product experiences in MEMS sensors, especially in special sensing technology. After joining Coretronic group in 2019, he has leveraged the group's energy in system integration and AI to provide total solution for AIoT smart manufacturing applications.



Kai-Chih Liang was born in Taipei, Taiwan, in 1979. He received the Ph.D. degree from the Department of Power Mechanical Engineering, National Tsing Hua University, Hsinchu, Taiwan, in 2020. His research interests include CMOS MEMS integration designs and multiple sensors integration. He has been with the TSMC MEMS Department, Hsinchu, since 2004, as the Principal Engineer for developing CMOS-MEMS platform and multiple sensors projects development into mass production. Afterthat, he joined the CoretronicMEMS, Hsinchu, in 2020, as the director of MEMS engineering and business development. He is current devoting himself in piezoelectric transducers development and marketing exploration for business engagement.



Mei-Feng Lai was born in Pingtung, Taiwan. She received her Ph.D. degree from National Taiwan University in 2005. Her doctoral research focused on the magnetization process of patterned permalloy nanostructures. She joined the Department of engineering science and ocean engineering at National Taiwan University in 2005, and then transferred to the Power Mechanical Engineering Department at National Tsing Hua University (Taiwan) in 2007, where she is now a professor as well as a faculty of NEMS Institute. Her research interests include magnetic sensors and actuators, spintronics, bioMEMS, soft matters, and so on.



Weileun Fang was born in Taipei, Taiwan. He received his Ph.D. degree from Carnegie Mellon University in 1995. His doctoral research focused on the determining of the mechanical properties of thin films using micro-machined structures. In 1995, he worked as a post-doctoral research at Synchrotron Radiation Research Center, Taiwan. He joined the Power Mechanical Engineering Department at the National Tsing Hua University (Taiwan) in 1996, where he is now a Chair Professor as well as a faculty of NEMS Institute. In 1999, he was with Prof. Y.-C. Tai at California Inst. Tech. as a visiting associate. He was elevated to IEEE Fellow in 2015 to recognize his contribution in MEMS area. His research interests include MEMS with emphasis on micro fabrication/packaging technologies, CMOS MEMS, PZT MEMS, micro optical systems, micro sensors and actuators, and characterization of thin film mechanical properties. He is now the Chief Editor of JMM, the Associate Editor of IEEE Sensors Journal, and the Board Member of the IEEE Transactions on Device and Materials Reliability. He served as the member of ISC (International steering committee) of Transducers in 2009–2017, and the ISC chair in 2017–2019. He also served as the General Chair of Transducers Conference in 2017. He was the TPC of IEEE MEMS and the EPC of Transducers for many years, and the Program Chair of IEEE Sensors Conference in 2012. He served as the Chief Delegate of Taiwan for the World Micromachine Summit (MMS) in 2008–2012, and the General Chair of MMS in 2012. Prof. Fang has close collaboration with MEMS industries and is now the Vice Chair of the MEMS and Sensors Committee of SEMI Taiwan.